IEEE Access, vol. 10, pp. 49 585–49 598, 2022

Detection of Broken Rotor Bars in a Cage Induction Machine Using DC Injection Braking

D. G. Jerkan, D. Reljić, I. Todorović, *et al.*

POWER ELECTRONICS LABORATORY
ÉCOLE POLYTECHNIQUE FÉDÉRALE DE LAUSANNE

IEEE Access
Multidisciplinary ⋮ Rapid Review ⋮ Open Access Journal

Received March 29, 2022, accepted May 2, 2022, date of publication May 9, 2022, date of current version May 12, 2022.

Digital Object Identifier 10.1109/ACCESS.2022.3173352

Detection of Broken Rotor Bars in a Cage Induction Machine Using DC Injection Braking

DEJAN G. JERKAN[1], (Member, IEEE), DEJAN RELJIĆ[1], (Member, IEEE), IVAN TODOROVIĆ[1], (Member, IEEE), IVANA ISAKOV[1], (Member, IEEE), VLADO POROBIĆ[1], (Member, IEEE), AND DRAŽEN DUJIĆ[2], (Senior Member, IEEE)

[1]Faculty of Technical Sciences, University of Novi Sad, 21000 Novi Sad, Serbia
[2]Power Electronics Laboratory, École Polytechnique Fédérale de Lausanne (EPFL), 1015 Lausanne, Switzerland

Corresponding author: Dejan G. Jerkan (dejan.jerkan@uns.ac.rs)

This work was supported in part by the Science Fund of the Republic of Serbia under Grant 6468497, and in part by the Ministry of Education, Science and Technological Development of the Republic of Serbia under Project 451-03-68/2022-14/200156.

ABSTRACT In this paper, an effective procedure for broken rotor bar (BRB) fault detection in a three-phase squirrel-cage induction machine (SCIM) is proposed. This approach relies on a motor current signature analysis (MCSA) by observing the specific fault-related current component generated by applying the DC injection braking method. Unlike the traditional MCSA, which is commonly focused on the detection of BRB sidebands around the fundamental current component, the proposed methodology introduces a new BRB feature in the current spectrum which makes it much easier for identification. The distinctive time-frequency evolution pattern of this feature provides the reliable identification of BRBs, even under no-load operating conditions, thus overcoming the major drawback of traditional MCSA-based methods. Fault severity classification is easily performed through the magnitude inspection of the BRB fault-related current component. In addition, the proposed approach does not require high-complexity signal processing algorithms to achieve reliable results. The proposed concept is presented theoretically, assisted by a magnetically coupled multiple circuit model of the SCIM, both with healthy and faulty rotor bars. Finally, the experimental tests validate the proposed methodology and demonstrate its effectiveness and usefulness.

INDEX TERMS Squirrel-cage induction machine, DC injection braking, broken rotor bar, fault detection.

I. INTRODUCTION

Three-phase squirrel-cage induction machines (SCIMs) are the most common type of electrical machines used in a variety of applications. They are prime movers in modern industrial and transportation systems, and are also accepted in the concept of distributed power generation.

Although SCIMs are highly reliable, they are still subjected to different types of faults, usually caused by unsuitable operating conditions, improper drive installation, and/or manufacturing defects. Many studies have been conducted to evaluate the reliability of SCIMs and to identify the main cause of their failure in industrial and commercial systems [1]–[6]. The majority of failures in low-power SCIMs are due to bearing problems, whereas the causes of downtime for high-power SCIMs are not only related to bearing issues but also to stator windings faults, as well as rotor problems.

The associate editor coordinating the review of this manuscript and approving it for publication was Binit Lukose.

Broken rotor bars (BRBs) and cracked end-rings represent up to 10% of the overall SCIM faults in industrial systems [4]–[7]. Although these are not the most prevalent fault types, and it takes a certain period of time for the machine to fail, it does require increased attention to prevent potentially catastrophic consequences as the fault evolves, as well as to avoid serious implications on the machine performance and huge maintenance costs, including economic losses [8].

Different non-invasive methods have been proposed in the literature for BRB and end-ring fault detection. The most popular method is based on the motor current signature analysis (MCSA). It is a frequency-domain signal-based analysis technique [9] that has been widely adopted in industrial systems [10], [11]. The approach of the conventional MCSA relies on the detection of specific harmonic components in the machine's current spectrum, caused by rotor cage irregularities (electrical and magnetic), that is, BRB and/or end-rings faults. As stated in [12], MCSA is the optimal choice for machines under steady-state operation and rated load

conditions. In this respect, the MCSA method is usually performed using the discrete Fourier transform (DFT), that is, the fast Fourier transform (FFT) algorithm, whereas the most prominent fault-related harmonic components are first-order sidebands located at frequencies of [12], [13]:

$$f_{brb} = (1 \pm 2s) f_s, \tag{1}$$

where s is the rotor slip per unit value, and f_s is the fundamental supply frequency. The magnitudes of these sideband components indicate fault severity levels.

However, the conventional MCSA method has certain drawbacks that can seriously affect the performance of fault detection systems. The reliability of the MCSA is significantly influenced by the operating conditions of the machine. This is particularly the case in near-zero slip conditions [14], where the spectral leakage of the current fundamental component submerges with the slip-dependent sideband components associated with BRBs, making them difficult to detect [12], [15]–[17]. In addition, the magnitudes of the components of interest are quite small under these operating conditions [15], [16], thus affecting fault identification accuracy. The spectral leakage problem becomes even more prominent in inverter-fed machines, especially at low switching frequencies, which is typical for high-power drives [18]. Another issue associated with the MCSA technique is related to the spectral resolution, which has to be sufficiently high to properly identify BRB fault components in the current spectrum [17], [19]. Finally, the mechanical power transmission mechanism of the drive and mechanical loads (such as pumps, fans, or compressors), as well as pulsating loads, can provoke components around the fundamental current which can be misinterpreted as BRB fault indicators [15], [20], [21], thus compromising the reliability of the method. In addition to the disadvantages of the conventional MCSA, the method is not applicable to SCIMs operating under time-varying load conditions [14].

Various approaches have been suggested to alleviate the problems associated with the conventional MCSA method. Many advanced signal-processing techniques have been proposed in the literature regarding the reduction of spectral leakage. Among them, the most commonly used are those intended to eliminate the influence of the strong fundamental component of the machine current signal. In this regard, mathematical transformations, such as the Hilbert transform (HT) [15], [22], the Teager-Kaiser energy operator (TKEO) [23], and the frequency-domain energy operator (FDEO) [24], have been used to extract the current envelope, accompanied by the FFT to exploit the BRB fault frequency components from the current envelope signal. Another alternative for the suppression of the main supply component, before its spectral decomposition, was proposed in [18] and [25], where the authors used a notch filter for current envelope extraction. Other studies have suggested spectral analysis of the square machine current signal [26], as well as the spectral decomposition of rectified machine current signals [17], [27].

When it comes to frequency resolution issues, subspace techniques, such as multiple signal classification (MUSIC) [26], [28], [29] and estimation of signal parameters via rotational invariance technique (ESPRIT) [29], [30], have attracted significant interest. These techniques are commonly used in combination with empirical mode decomposition (EMD) [31] or zoom [32] algorithms to reduce their computational complexity. Another alternative to recognize the fault-related frequency bands is to use correlated EMD technique [33].

Despite the MCSA performance improvement with the above-mentioned demodulation techniques, the reported results have revealed that the accurate detection of BRB fault-related components is not viable under no-load operating conditions. This is particularly true for high-power machines. Hence, another approach to steady-state MCSA was introduced in [28], [34], involving a zero-sequence machine's current spectrum analysis (ZSCA). Unlike the conventional MCSA method, which commonly relies on the detection of harmonic components described in (1), the authors in [34] observed the spectral components of the zero-sequence current (ZSC), which offers more reliable diagnostic potential. However, the ZSCA-based MCSA is only applicable to delta-connected SCIMs or star-connected SCIMs with a neutral line. Likewise, a BRBs diagnosis strategy based on zero-sequence signal injection was presented in [35]. Although the methodology is highly immune to variable load operating conditions, its main drawback is associated with the necessity to access the star-point of the machine. Furthermore, this method is not applicable to delta-connected SCIMs. Finally, it is worth mentioning that the application of steady-state MCSA is more problematic for inverter-fed machines because it is difficult to separate the frequencies of interest from the nearby components coming from the inverter side [18].

A transient MCSA (TMCSA) method represents a step toward a more effective machine diagnosis procedure. In contrast to the conventional MCSA, which is based on the assumption of stationary operating conditions, the TMCSA is suitable for BRB fault detection under nonstationary regimes [36]. The TMCSA method can identify not only the presence of the BRB fault signatures in the machine current signal (i.e. frequencies of the main sideband components given in (1)), but also their characteristic time-frequency evolution pattern during the machine transients [37], thereby greatly improving the reliability of the BRB fault detection process. Because the loading condition does not affect the magnitudes of the fault-related sidebands of the current fundamental, BRBs can be detected even under a no-load machine operation. In addition, the TMCSA is not influenced by load torque oscillations and supply voltage fluctuations.

The TMCSA method is typically applied to the start-up current signal for SCIMs with a direct online start [37], employing different mathematical time-frequency transformations for BRB feature extraction. Among them, the short-time Fourier transform (STFT) is the most frequently

used [38], or its variants, such as the Gabor transform (GT) [39], as well as advanced techniques, such as different forms of the wavelet transform (WT) [37], the Wigner-Ville distribution (WVD) [40], the Stockwell transform (ST) [41], and the Walsh–Hadamard transform [42]. Other methods include a combination of several time-frequency techniques [43], [44]. However, the TMCSA method is prone to the spectral resolution issue, which is a major obstacle for current monitoring during the start-up period [45]. This problem is particularly pronounced if the machine start-up period is relatively short, but also in inverter-fed machines. To overcome this problem, the authors of [46] proposed the application of the TMCSA method during the counter-current braking regime with a prolonged deceleration period. Nevertheless, this method requires an auxiliary power supply to provide low braking torque, thus increasing the complexity of the system.

When considering the application of TMCSA in inverter-fed SCIMs, it is much more difficult to identify the trajectories of BRB-related harmonic components in the time-frequency plane. As a result of the smooth machine start-up/slow-down process (imposed by the inverter), BRB-related sidebands are close to the fundamental current component, making their detection especially problematic [44]. A few solutions with promising results on this problem have been recently reported in [47]–[50], but at the cost of high computational complexity.

Despite the efforts made in the previously discussed papers, simple, accurate, and reliable BRB fault detection in the early stage and under the no-load operating condition of the SCIM remains challenging. This represents an even greater task for inverter-fed machines. In addition, fault analysis regarding severity assessment is unreliable when the machine operates with near-zero slip. To address these problems and fill the research gap, this paper proposes a novel and effective MCSA-based procedure for BRB fault diagnosis based on the DC injection braking of the SCIM. In contrast to the traditional MCSA approach, the proposed methodology introduces a new BRB-related component in the machine-current spectrum. This component is slip-independent and much easier to identify, even under no-load machine operating conditions, thus overcoming the key problems of the previously discussed MCSA-based methods. The main contributions of the proposed approach are summarised as follows:

1. During DC braking, the strong BRB fault-related current component becomes slip independent, thus enabling it to be easily extracted from the machine current signal using low-complexity signal processing techniques.
2. The diagnosis of BRBs is unaffected by SCIM load conditions (it can be performed even without a load coupled to the machine) and braking current value. This improves the diagnostic capability and provides greater BRB fault sensitivity of the MCSA method.
3. Fault severity quantification is easily performed through the magnitude inspection of the normalised fault-related current component. The value of this indicator depends only on the number of BRBs and is not influenced by the selected braking current or machine load.
4. This method can be applied to all the power ranges of both line-connected and inverter-fed SCIMs. The latter does not require additional equipment because the inverter can operate in rectifier mode.
5. Similar to the traditional MCSA-based approach, only one current sensor is required.

The reminder of this paper is organised as follows. In Section II, a theoretical analysis of the stator current spectrum under BRB fault and DC injection is discussed. To gain better insight into the mechanism of establishing a new BRB fault indicator, an advanced mathematical model of the SCIM was used. The concept of the novel BRB fault-detection method is introduced in Section III. The experimental results and verification of the proposed methodology for BRBs detection are provided on the SCIM laboratory test bench and are presented in Section IV. Finally, the conclusions are offered in Section V.

II. THEORETICAL ANALYSIS

In this section, a theoretical investigation of the SCIM stator current spectrum under a BRB fault and the DC injection braking method is presented.

A. MATHEMATICAL MODEL OF THE SCIM

A SCIM model was used to investigate the influence of the BRB on the stator current spectrum. The model is based on the magnetically coupled multiple circuit (MCMC) approach [46], where each rotor bar and end-ring segment of the rotor cage are considered. Using the vector matrix notation, the electrical subsystem of the SCIM in the natural *abc* reference frame is defined as follows:

$$\frac{\mathrm{d}}{\mathrm{dt}}\begin{bmatrix}\boldsymbol{\Psi}_s\\ \boldsymbol{\Psi}_r\end{bmatrix}=\begin{bmatrix}\boldsymbol{V}_s\\ \boldsymbol{V}_r\end{bmatrix}-\begin{bmatrix}\boldsymbol{R}_s & \mathbf{0}\\ \mathbf{0} & \boldsymbol{R}_r\end{bmatrix}\begin{bmatrix}\boldsymbol{I}_s\\ \boldsymbol{I}_r\end{bmatrix}, \tag{2}$$

$$\begin{bmatrix}\boldsymbol{I}_s\\ \boldsymbol{I}_r\end{bmatrix}=\begin{bmatrix}\boldsymbol{L}_{ss} & \boldsymbol{L}_{sr}\\ \boldsymbol{L}_{rs} & \boldsymbol{L}_{rr}\end{bmatrix}^{-1}\begin{bmatrix}\boldsymbol{\Psi}_{\mathbf{s}}\\ \boldsymbol{\Psi}_{\mathbf{r}}\end{bmatrix}, \tag{3}$$

where $\boldsymbol{\Psi}_s$ and $\boldsymbol{\Psi}_r$ are the total flux linkages of the stator and rotor windings, $\boldsymbol{V}_s$ and $\boldsymbol{V}_r$ are the stator and rotor voltage vectors, $\boldsymbol{I}_s$ and $\boldsymbol{I}_r$ are the stator and rotor current vectors, $\boldsymbol{R}_s$ and $\boldsymbol{R}_r$ are the stator and rotor resistance matrices, $\boldsymbol{L}_{ss}$ and $\boldsymbol{L}_{rr}$ are the self-inductance matrices of the stator and rotor windings, and $\boldsymbol{L}_{sr}$ and $\boldsymbol{L}_{rs}$ are stator-to-rotor and rotor-to-stator mutual inductance matrices, respectively. By combining (2) and (3), the voltage-balance equation can be expressed in the following form:

$$\frac{\mathrm{d}}{\mathrm{dt}}\begin{bmatrix}\boldsymbol{I}_s\\ \boldsymbol{I}_r\end{bmatrix}+\begin{bmatrix}\boldsymbol{L}_{ss} & \boldsymbol{L}_{sr}\\ \boldsymbol{L}_{rs} & \boldsymbol{L}_{rr}\end{bmatrix}^{-1}\frac{\mathrm{d}}{\mathrm{dt}}\begin{bmatrix}\boldsymbol{L}_{ss} & \boldsymbol{L}_{sr}\\ \boldsymbol{L}_{rs} & \boldsymbol{L}_{rr}\end{bmatrix}\begin{bmatrix}\boldsymbol{I}_s\\ \boldsymbol{I}_r\end{bmatrix}$$
$$+\begin{bmatrix}\boldsymbol{L}_{ss} & \boldsymbol{L}_{sr}\\ \boldsymbol{L}_{rs} & \boldsymbol{L}_{rr}\end{bmatrix}^{-1}\begin{bmatrix}\boldsymbol{R}_s & \mathbf{0}\\ \mathbf{0} & \boldsymbol{R}_r\end{bmatrix}\begin{bmatrix}\boldsymbol{I}_s\\ \boldsymbol{I}_r\end{bmatrix}$$

$$= \begin{bmatrix} \boldsymbol{L_{ss}} & \boldsymbol{L_{sr}} \\ \boldsymbol{L_{rs}} & \boldsymbol{L_{rr}} \end{bmatrix}^{-1} \begin{bmatrix} \boldsymbol{V_s} \\ \boldsymbol{V_r} \end{bmatrix}. \tag{4}$$

Stator and rotor voltage vectors are represented as follows [46]:

$$\boldsymbol{V_s} = \begin{bmatrix} v_a & v_b & v_c \end{bmatrix}^T, \tag{5}$$

$$\boldsymbol{V_r} = \begin{bmatrix} 0 & 0 & \dots & 0 & 0 \end{bmatrix}^T_{N_B+1}. \tag{6}$$

There are three stator voltages (v_a, v_b, v_c) for three phase windings, and (N_B+1) rotor voltages equal to zero (rotor has N_B bar loops, where N_B is the number of rotor bars, and two end-rings loops, i.e. there are (N_B+1) independent current loops in the rotor cage).

Stator and rotor current vectors are defined as [46]:

$$\boldsymbol{I_s} = \begin{bmatrix} i_a & i_b & i_c \end{bmatrix}^T, \tag{7}$$

$$\boldsymbol{I_r} = \begin{bmatrix} i_{rl1} & i_{rl2} & \dots & i_{rlN_B} & i_e \end{bmatrix}^T_{N_B+1}, \tag{8}$$

There are three stator currents (i_a, i_b, i_c) in three-phase windings, whereas the rotor current vector consists of N_B rotor loop currents ($i_{rl1}, i_{rl2}, \dots, i_{rlN_B}$) and one end-ring loop current (i_e).

The stator resistance matrix is a 3×3 diagonal matrix with elements that represent the phase resistance of the stator windings [46]:

$$\boldsymbol{R_s} = \begin{bmatrix} R_s & 0 & 0 \\ 0 & R_s & 0 \\ 0 & 0 & R_s \end{bmatrix}. \tag{9}$$

The rotor resistance matrix is a $(N_B+1)\times(N_B+1)$ symmetric matrix with elements that include each bar and end-ring segment resistance, and is expressed in general as (10), shown at the bottom of the page, [46], where R_{lk} is the rotor loop resistance ($1 \le k \le N_B$) defined as $R_{lk} = R_{bk} + R_{b(k+1)} + 2R_{ek}$, R_{bk} is the resistance of bar k ($R_{bk} = R_b$ for a healthy rotor cage), and R_{ek} is the resistance of the end-ring segment, denoted as k ($R_{ek} = R_e$ for a healthy rotor cage). Further details on the construction of the rotor resistance matrix can be found in [46].

Because the BRB fault causes an electrical imbalance in the rotor cage, the rotor resistance matrix should be modified to include any rotor bar defects. Hence, if a fault occurs in the k^{th} bar, then the resistance of that bar will increase, as will the resistance of other elements in the rotor resistance matrix affected by this fault. A detail in the rotor resistance matrix related to one partially BRB is demonstrated in (10), where elements denoted in red are affected by a defect of the bar k. Likewise, the rotor resistance matrix for more than one partially BRB can be constructed.

The rotor bar current (i_{bk}, $1 \le k \le N_B$) can be calculated from adjacent rotor loop currents as follows:

$$i_{bk} = i_{lk} - i_{l(k+1)}. \tag{11}$$

The stator self-inductance matrix is a 3×3 symmetric matrix with constant value elements [46]:

$$\boldsymbol{L_{ss}} = \begin{bmatrix} L_a & M_{ab} & M_{ac} \\ M_{ba} & L_b & M_{bc} \\ M_{ca} & M_{cb} & L_c \end{bmatrix}, \tag{12}$$

where L_a, L_b, and L_c are the self-inductances of the stator windings ($L_a = L_b = L_c$), and M_{ab}, M_{ba}, M_{bc}, M_{cb}, M_{ac}, and M_{ca} are the mutual inductances between the stator windings ($M_{ab} = M_{ba} = M_{bc} = M_{cb} = M_{ac} = M_{ca}$).

The rotor self-inductance matrix is a $(N_B+1) \times (N_B+1)$ symmetric matrix with constant value elements, and is formed as [46] (13), shown at the bottom of the next page, in which $L_{lk} = L_k + L_{bk} + L_{b(k+1)} + 2L_{ek}$, $1 \le k \le N_B$, L_k is self-inductance of the loop k, L_{bk} is leakage inductance of the rotor bar k, and L_{ek} is leakage inductance of the rotor end-ring segment k. Mutual inductances between arbitrary rotor loops m and n are denoted as M_{rmn} ($1 \le m, n \le N_B \bigwedge m \ne n$). For a healthy machine and a machine with partially BRBs, $L_{lk} = L_l$ and $L_{ek} = L_e$.

$$\boldsymbol{R_r} = \begin{bmatrix}
R_{l1} & -R_{b2} & 0 & \dots & \dots & \dots & \dots & \dots & \dots & -R_{bN_B} & -R_{e1} \\
-R_{b1} & R_{l2} & -R_{b3} & 0 & \dots & \dots & \dots & \dots & \dots & 0 & -R_{e2} \\
0 & -R_{b2} & R_{l3} & -R_{b4} & \dots & \dots & \dots & \dots & \dots & 0 & -R_{e3} \\
\vdots & 0 & \vdots & \ddots & \ddots & \ddots & \ddots & \ddots & \ddots & \vdots & \vdots \\
\vdots & \vdots & \vdots & \dots & R_{l(k-1)} & -R_{bk} & 0 & \dots & \dots & \vdots & \vdots \\
\vdots & \vdots & \vdots & \dots & -R_{b(k-1)} & R_{lk} & -R_{b(k+1)} & 0 & \dots & \vdots & \vdots \\
\vdots & \vdots & \vdots & \dots & 0 & -R_{bk} & R_{l(k+1)} & -R_{b(k+2)} & \ddots & \vdots & \vdots \\
\vdots & \vdots & \vdots & \dots & \vdots & 0 & \ddots & \ddots & \ddots & \vdots & \vdots \\
0 & 0 & \dots & \dots & \dots & \dots & \dots & \dots & \dots & -R_{bN_B} & -R_{e(N_B-1)} \\
-R_{b1} & 0 & \dots & \dots & \dots & \dots & \dots & \dots & \dots & R_{lN_B} & -R_{eN_B} \\
-R_{e1} & -R_{e2} & \cdots & \dots & \dots & \dots & \dots & \dots & \dots & -R_{eN_B} & \sum_{i=1}^{N_B} R_{ei}
\end{bmatrix}. \tag{10}$$

The stator-to-rotor mutual inductance matrix is $3\times(N_B+1)$ matrix expressed as [46]:

$$\boldsymbol{L_{sr}} = \begin{bmatrix} M_{al1}(\vartheta) & M_{al2}(\vartheta) & \dots & M_{al_{N_B}}(\vartheta) & 0 \\ M_{bl1}(\vartheta) & M_{bl2}(\vartheta) & \dots & M_{bl_{N_B}}(\vartheta) & 0 \\ M_{cl1}(\vartheta) & M_{cl2}(\vartheta) & \dots & M_{cl_{N_B}}(\vartheta) & 0 \end{bmatrix}, \tag{14}$$

where $\boldsymbol{L_{rs}} = \boldsymbol{L_{sr}^T}$ holds. The mutual inductances between any stator phase winding and rotor loop in (14) are denoted as M_{xlk}, $x \in \{a, b, c\}, 1 \leq k \leq N_B$. These mutual inductances are complex periodic functions of rotor electrical angular position ϑ, but without the loss of generality, they can be approximated as simply periodic (sine harmonic function). The arguments of the periodic functions within adjacent elements in the same row of the stator-to-rotor mutual inductance matrix have an angular displacement of $\alpha = 2\pi/N_B$ electrical degrees. A similar is valid for adjacent elements in the same column of the stator-to-rotor mutual inductance matrix, with the difference that the arguments of periodic functions now have an angular displacement of $2\pi/3$ electrical degrees. The last column of the stator-to-rotor mutual inductance matrix has zero values because there is no magnetic coupling between the stator phase windings and rotor end-rings. The elements of the inductance matrices in (12)–(14) can be calculated using several approaches; the finite-element method (FEM) is used in this paper.

The equation of the electromagnetic torque is stated as follows [46]:

$$T_e = \frac{1}{2}p \begin{bmatrix} \boldsymbol{I_s} \\ \boldsymbol{I_r} \end{bmatrix}^T \begin{bmatrix} \boldsymbol{0} & \frac{d}{d\vartheta}(\boldsymbol{L_{sr}}) \\ \frac{d}{d\vartheta}(\boldsymbol{L_{rs}}) & \boldsymbol{0} \end{bmatrix} \begin{bmatrix} \boldsymbol{I_s} \\ \boldsymbol{I_r} \end{bmatrix}, \tag{15}$$

where p is the number of pole pairs.

The model of mechanical subsystem is given by Newton differential equation of motion:

$$J\frac{d\omega_m}{dt} = T_e - T_L, \tag{16}$$

where T_L denotes the load torque, J denotes the total moment of inertia, and ω_m denotes the rotor mechanical speed. The equation for the rotor mechanical speed is:

$$\omega_m = \frac{1}{p}\frac{d\vartheta}{dt}. \tag{17}$$

Finally, the general model of SCIM based on the MCMC approach is defined using (4)–(17). The model is derived by including the following basic approximations: the iron losses are neglected, ferromagnetic materials are considered linear, and inter-bar currents are neglected. These assumptions did not cause significant deviations in the results.

B. CURRENT DISTRIBUTION IN THE ROTOR BARS

Once the SCIM model is established, the next step is to provide a deeper insight into the phenomena introduced by the BRB fault in the braking mode employing DC injection.

The DC injection braking method provides braking action by applying a DC voltage to the stator windings (after the AC voltage has been previously disconnected). As a result, a stationary magnetic field is created. Owing to its interaction with the rotor magnetic field, braking torque is produced, which acts on the rotor to align it with the stator magnetic field. The braking torque is adjusted by controlling the stator current via the applied DC voltage. The DC source is connected across two or three stator terminals. A DC injection braking scheme with delta-connected stator windings is illustrated in Fig. 1. A DC voltage is applied across the two stator terminals (other arrangements of stator windings can also be used). Accordingly, as shown in Fig. 1, the voltage of phase a is the same as the input voltage of V_{DC}, whereas voltages across phases b and c are equal to $-(1/2)V_{DC}$. These phase voltages are further used in (5), that is, in the previously established mathematical model of the SCIM.

The machine considered in this paper is a three-phase delta-connected four-pole SCIM with 28 rotor bars and 36 stator slots. The BRB fault is modelled by increasing the resistance value of the faulty rotor bar as well as the resistance of other elements in (10) affected by the fault. To simplify the analysis, the developed SCIM model is used to simulate the steady-state machine operation with DC injection by forcing the rotor speed in (16) to be constant (the rotor maintains a rotational speed equal to the speed of the machine supplied with three-phase AC voltage). In addition, it is assumed that

$$\boldsymbol{L_{rr}} = \begin{bmatrix} L_{l1} & \cdots & M_{r1\,N_B} - L_{bN_B} & -L_{e1} \\ M_{r21} - L_{b1} & \ddots & M_{r2\,N_B} & -L_{e2} \\ \vdots & \cdots & \vdots & \vdots \\ \vdots & \cdots & \vdots & \vdots \\ M_{r(N_B-1)1} & \cdots & M_{r(N_B-1)N_B} - L_{bN_B} & -L_{e(N_B-1)} \\ M_{rN_B1} - L_{b1} & \cdots & L_{lN_B} & -L_{eN_B} \\ -L_{e1} & \cdots & -L_{eN_B} & \sum_{i=1}^{N_B} L_{ei} \end{bmatrix}, \tag{13}$$

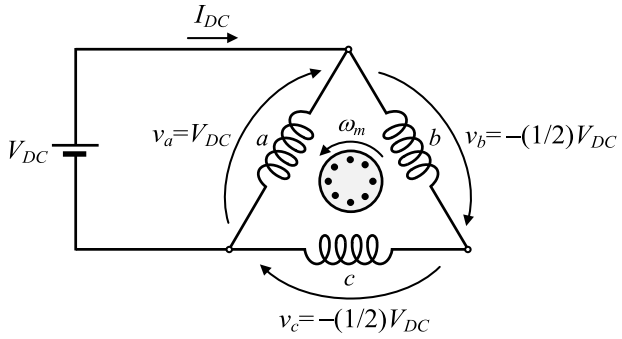

FIGURE 1. DC injection braking scheme (DC voltage is applied across two stator terminals, with the third kept open).

before applying the DC injection, the machine has not been connected to any load; thus, the rotor mechanical speed is equal to the machine's synchronous speed ω_{ms} (mechanical losses have been neglected). Hence, the influence of the BRB fault on the current distribution in the rotor bars is easily observable.

The computer simulation of the SCIM model under DC injection and a constant rotor speed of 50π rad/s was performed using the MATLAB/Simulink software. The results of the rotor bar current distribution for healthy and faulty rotor cage conditions are presented in Fig. 2, whereas the rotor bar current phasors are depicted in Fig. 3. As exhibited in Fig. 2(a), the current distribution in the bars of the healthy rotor cage was uniform, resulting in a symmetrical current regime (Fig. 3(a)). In contrast, the results obtained for a faulted rotor cage with a partially BRB (the 10^{th} bar was selected as the faulty one) exposed an uneven current distribution in the rotor bars (Fig. 2(b)). The current amplitudes in the 9^{th} and 11^{th} rotor bars significantly increase with respect to the healthy rotor state. The unbalanced rotor circuit yields an asymmetrical rotor current regime, as shown in Fig. 3(b).

C. INFLUENCE OF THE BRB FAULT ON THE STATOR CURRENT UNDER DC INJECTION

The previous subsection provided an insight into the current distribution of the rotor bars for both the healthy rotor cage and the rotor cage affected by the BRB fault, simulated under DC injection and constant rotor speed. Further analysis was extended by introducing the symmetrical components [46]. Through the Fortescue transformation applied to the phasor representation of the rotor bar currents (Fig. 3), one can obtain the symmetrical components of the rotor bars multiphase current system, (Fig. 4). The symmetrical set of rotor current phasors shown in Fig. 3(a) contains only the first symmetrical component, as presented in Fig. 4(a). It is a so-called direct-order component that represents the symmetrical regime of a balanced multiphase rotor electrical circuit.

The asymmetrical set of phasors in Fig. 3(b), on the other hand, results in additional symmetrical components. More precisely, in addition to the first symmetrical component, the 27^{th} order symmetrical component is emphasized (Fig. 4(b)).

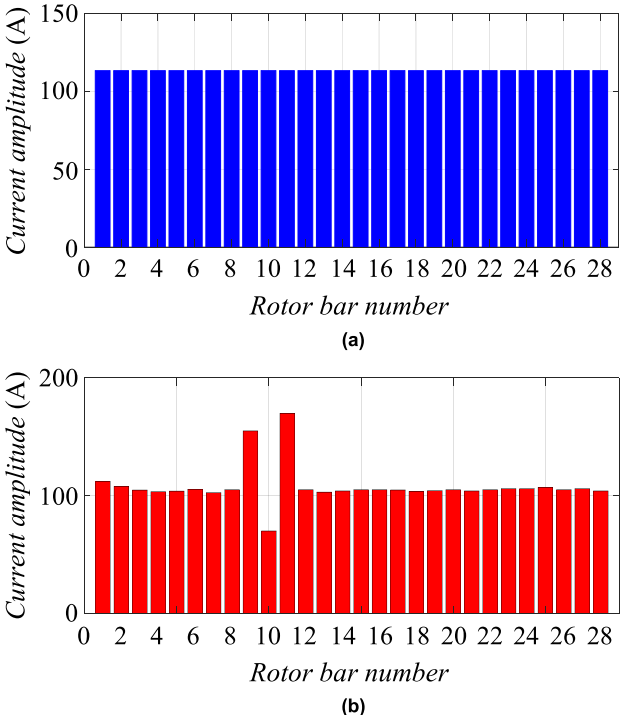

FIGURE 2. Rotor bar current amplitude distribution under DC injection and constant rotor mechanical speed of 50π rad/s. (a) Healthy machine. (b) Faulty machine with a partially BRB No. 10.

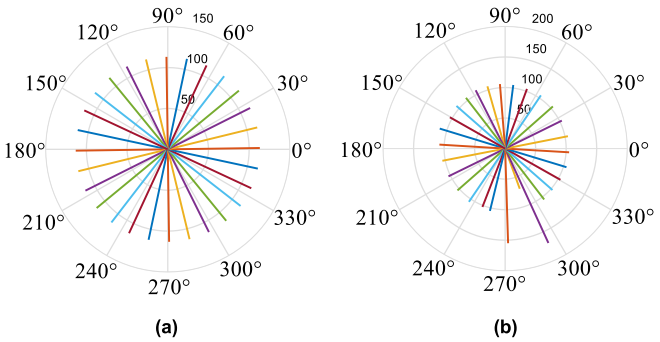

FIGURE 3. Polar diagram of rotor bar current phasors under DC injection and constant rotor mechanical speed of 50π rad/s. (a) Healthy machine. (b) Faulty machine with a partially BRB No. 10.

This is a component of order $(N_B - 1)$. It is noteworthy that the set of components that belong to the symmetrical component of order $(N_B - 1)$ has an angular displacement of $(N_B - 1)(2\pi/N_B)$, which is equivalent to $-2\pi/N_B$, i.e. $-2\pi/28$. Therefore, the symmetrical component of the 27^{th} order can be considered as an inverse-order component. This component was expected to be reflected in the stator current. This can be demonstrated analytically.

As previously demonstrated, the BRB fault causes inverse-order symmetrical components in the rotor bar currents (Fig. 4(b)) and hence in the rotor bar loops. Owing to the magnetic coupling between the stator and rotor electrical circuits, a part of the stator phase a flux linkage

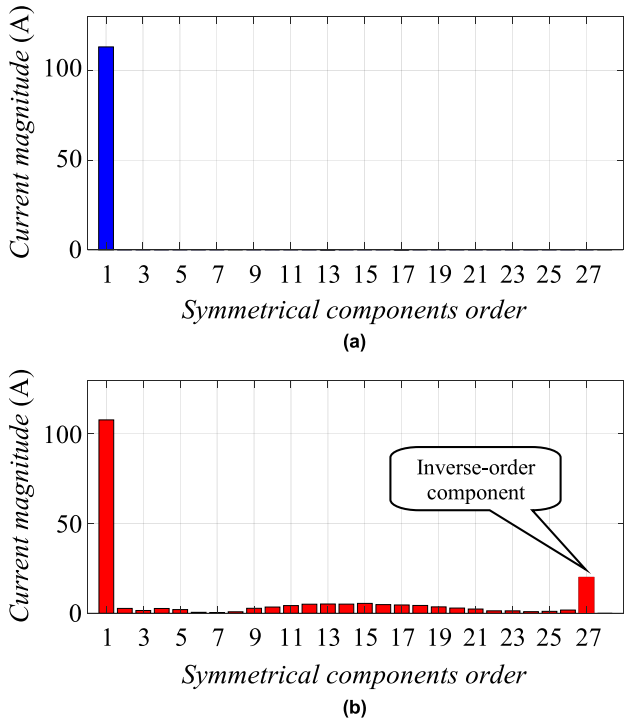

FIGURE 4. Symmetrical components of the rotor bar multiphase current system. (a) Healthy machine. (b) Faulty machine with a partially BRB No. 10.

can be expressed as:

$$\Psi_{ai} = \sum_{k=1}^{N_B} M_{alk}(\vartheta) i_{lik}^{sym}, \tag{18}$$

where the inversed-order current in the rotor loop k is labelled with i_{lik}^{sym}.

By varying the stator-rotor mutual inductance, in a sinusoidal manner as a function of the rotor electrical angular position ϑ, the expression (18) can be further developed as:

$$\Psi_{ai} = \sum_{k=1}^{N_B} \left\{ \begin{matrix} M_{alk} \cos\left(\vartheta - \frac{(k-1)2\pi}{N_B}\right) \cdot \\ I_{li}^{sym} \cos\left(\omega_r t + \frac{(k-1)2\pi}{N_B}\right) \end{matrix} \right\}. \tag{19}$$

No generality is lost by ignoring the initial phase angles in the arguments of the mutual inductance and rotor loop current functions in (19). The angular frequency of the rotor currents is denoted as ω_r, whereas I_{li}^{sym} represents the amplitude of the inverse-order currents in the rotor loops. Note that only inverse-order symmetrical components are used in (19); thus, different signs of phase angles are used in the arguments of stator-rotor inductance and rotor loop current functions.

Rotor electrical angular position is proportional to the rotor electrical angular speed:

$$\vartheta = p\vartheta_m = p\left(\omega_m t + \vartheta_{m0}\right) = \omega_{elr} t + \vartheta_0, \tag{20}$$

where ω_{elr} represents rotor electrical angular speed, and ϑ_{m0} is the initial electrical position of the rotor. During DC injection, the stator windings produce a stationary magnetic field; however, owing to machine rotation, it acts as an alternating field for the rotor electrical circuit. Thus, the angular frequency of the rotor currents is:

$$\omega_r = p\omega_m = \omega_{elr}. \tag{21}$$

An interesting feature of the DC injection method was observed according to (20) and (21). Namely, because the stator-to-rotor mutual inductances in (14), as well as in (19), depend on the rotor electrical angular position, they are also a function of angular frequency of rotor currents. By substituting (20) and (21) into (19), we obtain:

$$\Psi_{ai} = \sum_{k=1}^{N_B} \left\{ \begin{matrix} M_{alk} \cos\left(\omega_{elr} t - \frac{(k-1)2\pi}{N_B} + \vartheta_0\right) \cdot \\ I_{li}^{sym} \cos\left(\omega_{elr} t + \frac{(k-1)2\pi}{N_B}\right) \end{matrix} \right\}. \tag{22}$$

Using basic trigonometric transformations, (22) is further transformed:

$$\Psi_{ai} = \sum_{k=1}^{N_B} \frac{I_{li}^{sym} \cdot M_{alk}}{2} \left\{ \begin{matrix} \cos\left(2\omega_{elr} t + \vartheta_0\right) + \\ \cos\left(\frac{(k-1)4\pi}{N_B} - \vartheta_0\right) \end{matrix} \right\}. \tag{23}$$

After finding sums of components in (23), the following is obtained:

$$\Psi_{ai} = N_B \frac{I_{li}^{sym} \cdot M_{alk}}{2} \cos\left(2\omega_{elr} t + \vartheta_0\right). \tag{24}$$

Similarly, a part of the flux linkage for the other two stator windings (b and c) can be derived as follows:

$$\Psi_{bi} = N_B \frac{I_{li}^{sym} \cdot M_{alk}}{2} \cos\left(2\omega_{elr} t + \vartheta_0 - \frac{2\pi}{3}\right), \tag{25}$$

$$\Psi_{ci} = N_B \frac{I_{li}^{sym} \cdot M_{alk}}{2} \cos\left(2\omega_{elr} t + \vartheta_0 + \frac{2\pi}{3}\right). \tag{26}$$

Based on (24)–(26), it is evident that the flux linkages of the stator windings involve fault-dependent components at an angular frequency of $2\omega_{elr}$. These components affect the stator windings by imposing a stator current component with the same angular frequency. Therefore, it can be concluded that, under DC injection, the frequency of the BRB-related component in the stator current is exactly twice the rotor electrical rotation frequency.

The analytical approach was further validated by computer simulation. The simulated stator currents of the healthy and faulty SCIMs with a partially BRB are presented in Fig. 5 and Fig. 6. According to the simulation results of the DC injection method for the healthy machine, the stator current contains only a DC component. This is clearly visible in Fig. 5(a) and Fig. 5(b), where the waveform and spectrum of the stator current are presented, respectively. However, when considering the DC injection method under faulty rotor cage conditions, oscillations are experienced in the stator current (Fig. 6(a)). This can be easily identified through the stator current spectrum analysis, as shown in Fig. 6(b). The oscillation frequency is equal to twice the electrical rotational frequency of the rotor. It was 100 Hz for a given rotor mechanical angular speed of 50π rad/s and two pole pairs of the machine under investigation. According to theoretical analysis, the BRB-related component in the stator current

spectrum appears at the same frequency. This leads to the conclusion that the simulation results are consistent with the theoretical analysis.

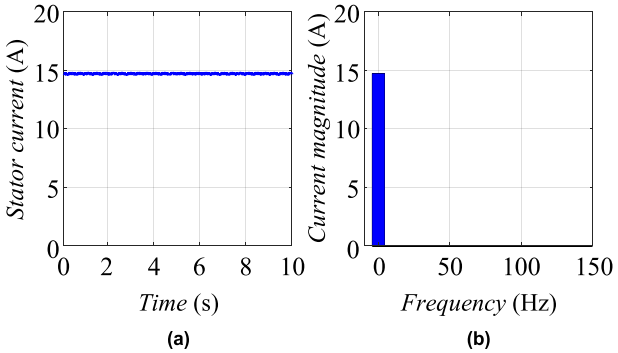

FIGURE 5. Stator current of the healthy machine under DC injection and constant rotor mechanical speed of 50π rad/s. (a) Time-domain representation. (b) Frequency-domain representation.

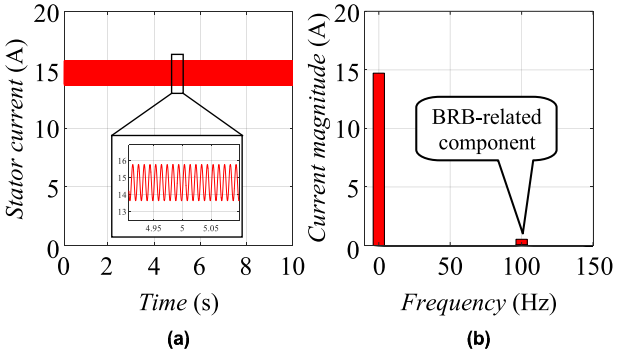

FIGURE 6. Stator current of the faulty machine (partially BRB No. 10) under DC injection and constant rotor mechanical speed of 50π rad/s. (a) Time-domain representation. (b) Frequency-domain representation.

III. THE NOVEL METHOD FOR BRBs DETECTION

The previous sections provided a theoretical foundation for the formulation of a novel method for BRB fault detection. The fundamental basis of this method is the BRB-related component in the stator current spectra during the DC injection braking procedure with an angular instantaneous frequency of $2\omega_{elr}$. For convenience, the same component can be represented with a frequency of $2f_{elr}$, where $\omega_{elr} = 2\pi f_{elr}$ holds. Since the braking procedure is transient, the electrical frequency of the rotation f_{elr} is also time-varying.

The DC injection braking should be performed as follows. At the beginning of the test, the unloaded/loaded SCIM, supplied by the inverter, is accelerated to a certain speed (preferably nearly rated synchronous speed, though not necessary) and then switched to the inverter's built-in DC current braking mode (the actual DC braking current value can, of course, be set at the desired value prior to the test procedure, using the inverter's interface). The inverter starts to supply stator windings with DC currents, which leads to the generation of braking torque, the intensity of which is directly proportional to the injected DC current. The braking torque begins to slow down the rotor, eventually leading to the complete halt of the motor. During this braking period, the stator windings through magnetic coupling with the rotor electrical circuits experience a high and stable rotor response (relative to the stator DC current), which is visible in the time-varying harmonic component at the frequency $2f_{elr}$. During the DC injection braking test, the fundamental component of the stator currents is at zero frequency; thus, it allows an easy separation of the BRB-related current component, whose frequency varies with time as the rotor speed decreases. Additionally, other speed-variable harmonics may exist in the stator current spectra (mainly slot harmonics or harmonics generated by the DC voltage source converter). However, their frequencies are higher than the BRB fault-related frequency $2f_{elr}$, and will not affect the BRB fault detection procedure. The broken bar fault creates a unique pattern in the time-frequency plane of the current signal. Based on (24)–(26), and under the assumption that the supply frequency prior to the start of the DC braking was 50 Hz, and that the SCIM was at no-load, at the beginning of the test, the frequency of the fault-induced current component is approximately 100 Hz. As the rotor speed decreased, the frequency decreased down to 0 Hz at the end of the braking process. The corresponding frequency evolution pattern of the BRB-related current component is displayed in Fig. 7.

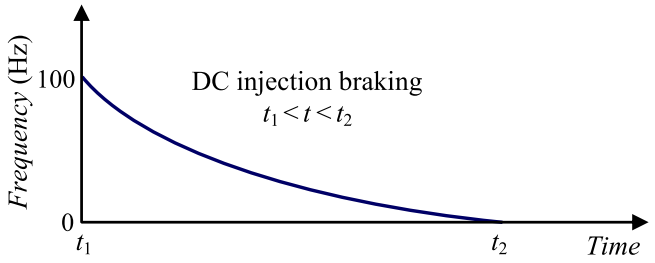

FIGURE 7. The frequency evolution pattern of the fault-induced current component considering the supply frequency of 50 Hz prior to the braking, and the beginning of the DC injection braking at the no-load speed close to ω_{ms}.

It is important to state that the SCIM does not need to be at the no-load condition to perform the proposed test procedure. If the machine is loaded before the beginning of the DC injection braking, the rotor electrical speed will be significantly lower than synchronous speed; thus, the starting frequency f_{elr0} will not be equal to 50 Hz. The frequency f_{elr0} will be slightly lower than the synchronous speed frequency and will depend on the loading level, i.e. the slip value at the instant of switching the machine to the DC injection braking:

$$f_{elr0} = (1 - s) \cdot f_s = (1 - s) \cdot 50 \text{ [Hz]}. \tag{27}$$

The DC braking test performed on the loaded SCIM will last shorter than the same test on the unloaded SCIM, which may affect an acquisition period. In this case, it is necessary to apply a DC braking current with a lower value. However, one of the advantages of the proposed method is that the

relative amplitudes of the BRB-related spectral components are independent of the applied values of the DC braking currents, which means that it is quite feasible to lower the value of the braking currents to provide an adequate acquisition period in the case of the loaded SCIM.

A technique for nonstationary signal analysis has to be used to obtain the time-frequency representation of the phase current signal. STFT is one of the most straightforward approaches and was applied in this paper. The STFT results are presented in the form of a spectrogram in which the fault-induced current component and its pattern can be easily observed. The STFT spectrogram is usually shown as a plot in which the time-frequency axis is in the horizontal plane, and the vertical axis represents the magnitude (normalised to the DC fundamental component and expressed in dB) of the stator phase current signal spectra. The colour map indicates the magnitude of a specific frequency at a specific time instant.

IV. EXPERIMENTAL RESULTS

To verify the proposed method, an experimental test bench was constructed, as depicted in Fig. 8. The test bench consists of a three-phase SCIM under test (marked as 1), industrial inverter Danfoss VLT FC 302 (marked as 2), current probe Tektronix A622 (marked as 3), high-performance data acquisition card NI USB-6251 (marked as 4), and laptop computer (marked as 5). The other elements include interchangeable rotors (marked as 6), one with a healthy rotor cage (located inside the stator of the SCIM under test) with 28 bars, and three faulty rotors (one partially broken bar, and one and three contiguous fully broken bars) with the same number of rotor bars. These rotors were used with the stator of the SCIM under test (marked as 1). The BRB fault conditions were provoked by drilling rotor slots, as shown in Fig. 9. The partially broken bar was created by drilling a hole with 6 mm of diameter and 5 mm of depth (Fig. 9(b)), while one and three broken bars were generated by drilling holes through the whole depth of rotor slots (22 mm), Fig. 9(c) and Fig. 9(d). The three-phase SCIM under test has the following rated data: 11 kW, 400 V, 22 A, 50 Hz, and 1454 rpm.

The experimental time scheduler is presented in Fig. 10. In order to test and verify the ability of the proposed method, all experiments were carried out under no-load conditions. Note that this makes BRB fault detection even more difficult. The inverter power supply was used to perform a complete series of experimental tests on the SCIM. At the beginning of the tests, the SCIM was supplied with rated voltage and frequency. Therefore, it was ensured that the motor reached an almost synchronous speed prior to the start of the DC injection braking test. After the successful completion of the starting process, the DC injection braking procedure was initiated via the inverter interface using an on-board touch panel. During this phase, the inverter was operating as a controlled rectifier. Consequently, the motor began to decelerate.

The data acquisition process was performed during the braking period (the time between t_1 and t_2 as illustrated in Fig. 10). Only one motor-phase current was measured. The switching frequency of the VLT FC 302 power supply inverter was set to 4 kHz. To avoid frequency aliasing and to improve resolution, the motor current signal was sampled at a frequency of 12.8 kS/s, using the 16-bit A/D converter available at the NI USB-6251 data acquisition card. Thus, unambiguous data were ensured without using an analogue low-pass filter.

After the completion of the data acquisition process, STFT was performed using the Hamming window function to minimise spectral leakage. As a result, a time-varying spectrum was obtained, that is, the magnitudes of the time-varying

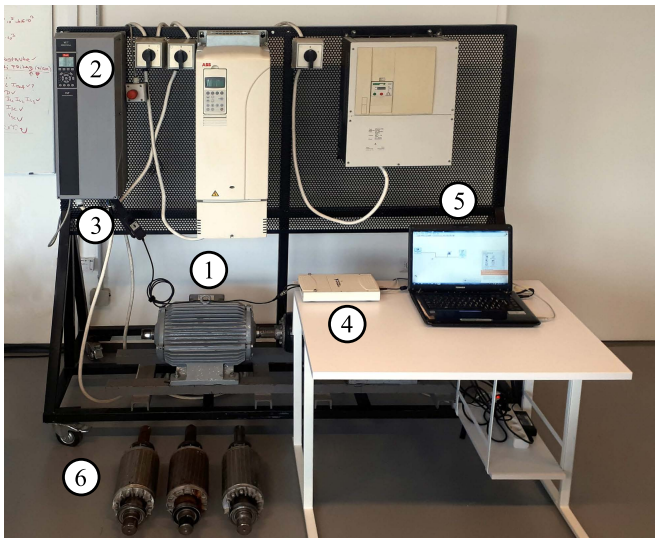

FIGURE 8. Experimental test bench for the BRB fault detection (1) SCIM under test, 2) industrial inverter, 3) current probe, 4) data acquisition card, 5) laptop computer, and 6) interchangeable cage rotors with different BRB severity).

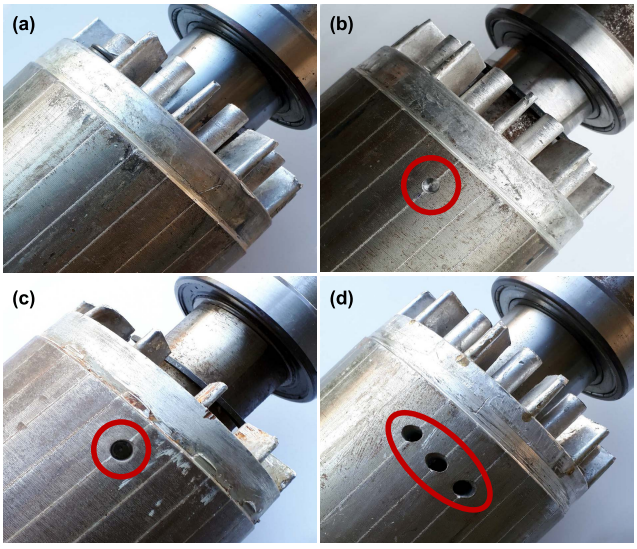

FIGURE 9. Interchangeable cage rotors. (a) Rotor with a healthy cage. (b) Rotor with one partially broken bar. (c) Rotor with one fully broken bar. (d) Rotor with three fully broken bars.

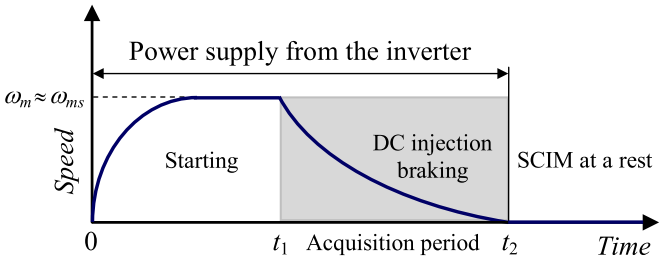

FIGURE 10. Experimental time scheduler for the SCIM under test.

current harmonic components were plotted on the time-frequency plane.

For each level of the BRB fault severity, three different experiments were conducted: with DC injection currents of 5 A, 10 A, and 15 A. This was performed to prove that the BRB-related spectral component has the same relative magnitude irrespective of the braking current values. Different braking current values, however, may have a major impact on the duration of the braking process, thus influencing the acquisition period.

The STFT current spectrograms obtained for a healthy rotor with three different braking current values (5 A, 10 A, and 15 A) are presented in Fig. 11, Fig. 12, and Fig. 13, respectively. During the DC injection braking period, BRB-related spectral components with very low magnitudes (approximately −89 dB on average) are visible in Fig. 11, Fig. 12, and Fig. 13. The existence of these components is due to fabrication imperfections in the squirrel-cage, which cannot be produced to meet the demands of a theoretically perfectly balanced electrical circuit. Nevertheless, these BRB-related components are practically negligible and may be used to set thresholds for SCIM with healthy rotor cage.

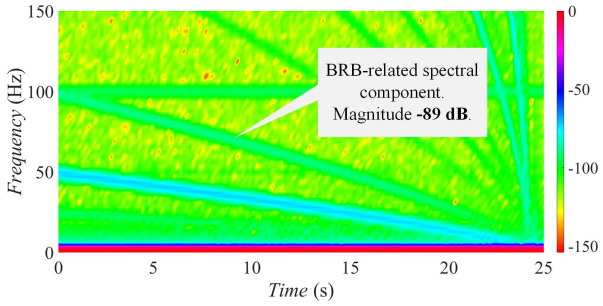

FIGURE 11. STFT current spectrogram of the healthy machine (no broken bars). DC injection current was set to 5 A.

The second set of experiments was performed on the SCIM with one partially BRB. The corresponding STFT current spectrograms with three different braking current values (5 A, 10 A, and 15 A) are shown in Fig. 14, Fig. 15, and Fig. 16. After analysing the obtained results, it becomes clear that the BRB-related spectral components follow the specific frequency pattern evolution associated with a faulty rotor cage condition, as presented in Fig. 7. This is in good agreement

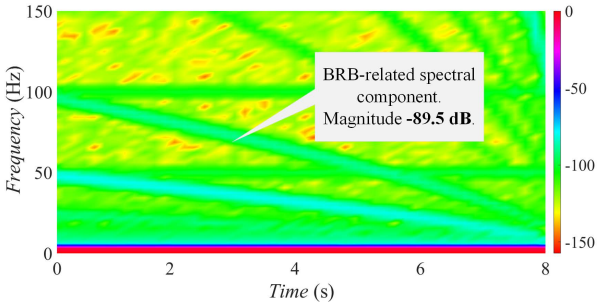

FIGURE 12. STFT current spectrogram of the healthy machine (no broken bars). DC injection current was set to 10 A.

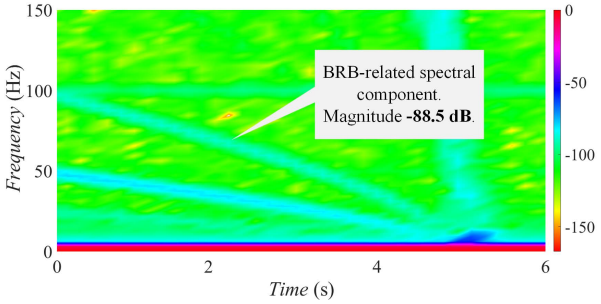

FIGURE 13. STFT current spectrogram of the healthy machine (no broken bars). DC injection current was set to 15 A.

with the theoretical analysis. The average magnitude of BRB-related current components is approximately −56.5 dB, which represents a significant increase compared with the magnitudes of these components in the case of a healthy rotor cage (Fig. 11, Fig. 12, and Fig. 13). Such a leap in the magnitudes of fault-related current spectral components proves that the proposed method is highly sensitive, even to one partially BRB. Note that the incipient BRB detection is crucial for an early BRB fault detection.

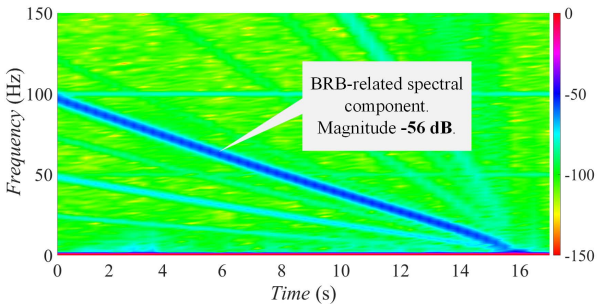

FIGURE 14. STFT current spectrogram of the faulty machine (one partially broken bar). DC injection current was set to 5 A.

To validate the proposed method further, the third set of experiments was performed on the same SCIM but with one fully BRB. The corresponding STFT current spectrograms with three different braking current values (5 A, 10 A, and 15 A) are presented in Fig. 17, Fig. 18, and Fig. 19, respectively. The BRB-related spectral components follow

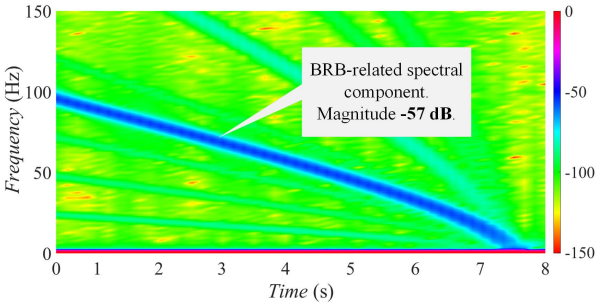

FIGURE 15. STFT current spectrogram of the faulty machine (one partially broken bar). DC injection current was set to 10 A.

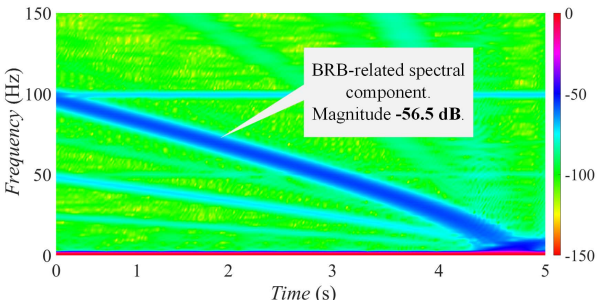

FIGURE 16. STFT current spectrogram of the faulty machine (one partially broken bar). DC injection current was set to 15 A.

the theoretically predicted frequency evolution pattern. The average magnitude of these BRB-related components is approximately −40 dB, and is much greater compared with the magnitudes of these components in the case of a healthy rotor cage (Fig. 11, Fig. 12, and Fig. 13) and a rotor cage with one partially BRB (Fig. 14, Fig. 15, and Fig. 16). This clearly indicates that the proposed method can be used for a reliable BRB fault detection, even when the breakage of only one rotor bar occurs.

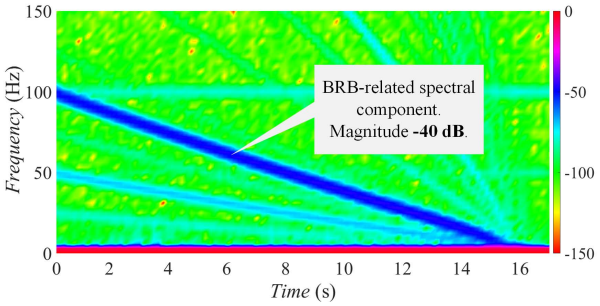

FIGURE 17. STFT current spectrogram of the faulty machine (with one broken bar). DC injection current was set to 5 A.

Finally, the SCIM with three fully BRBs was tested in the fourth set of experiments. The corresponding STFT current spectrograms are displayed in Fig. 20, Fig. 21, and Fig. 22. The specific frequency evolution pattern is clearly visible in the time-frequency plane, while magnitudes of the BRB-related current spectral components are even more prominent.

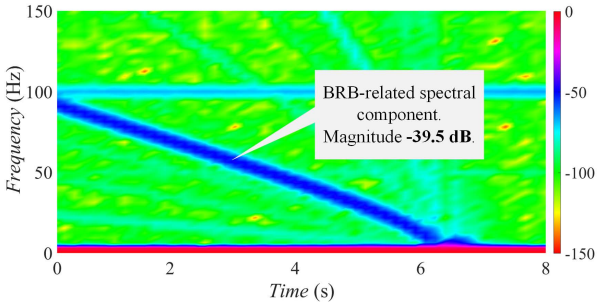

FIGURE 18. STFT current spectrogram of the faulty machine (with one broken bar). DC injection current was set to 10 A.

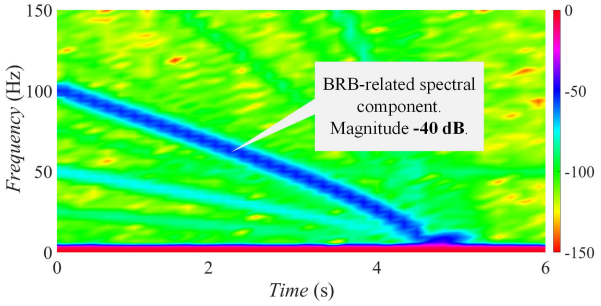

FIGURE 19. STFT current spectrogram of the faulty machine (with one broken bar). DC injection current was set to 15 A.

In this case, the magnitudes of the BRB-related components are significantly increased in comparison with the magnitudes of these components in the case of a healthy rotor cage, rotor cage with one partially broken bar, and rotor cage with one fully broken bar. Their average magnitude is now approximately −23 dB, which is a clear indication of multiple BRBs.

It is important to note that the experimental results have proved that DC injection current values hardly affect magnitudes of BRB components. Namely, their normalised magnitudes remain almost constant for the same BRB fault severity, irrespective of DC injection current values.

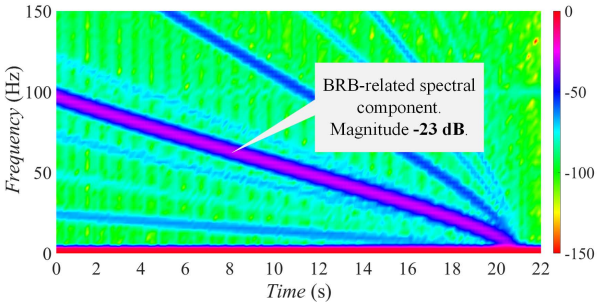

FIGURE 20. STFT current spectrogram of the faulty machine (with three broken bars). DC injection current was set to 5 A.

The results obtained from the previous experimental tests proved that the current component related to the BRBs could be easily recognised in the current spectra. Moreover, it can

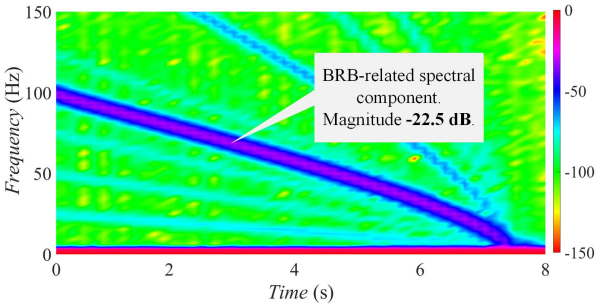

FIGURE 21. STFT current spectrogram of the faulty machine (with three broken bars). DC injection current was set to 10 A.

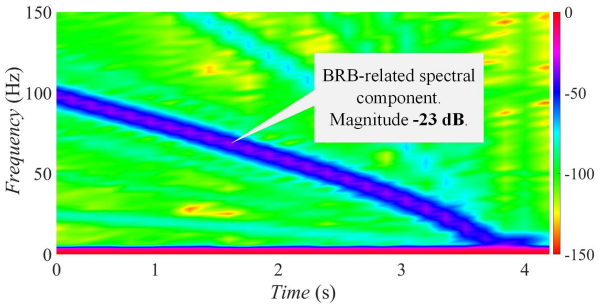

FIGURE 22. STFT current spectrogram of the faulty machine (with three broken bars). DC injection current was set to 15 A.

be observed that the magnitude of the BRB current component significantly increases with the number of broken bars. Finally, the proposed method is not influenced by the DC injection braking current values. All three DC braking current values cause almost the same value of the normalised fault-induced stator current component, with magnitudes of approximately −89 dB for the healthy rotor, −56.5 dB for the rotor with one partially broken bar, −40 dB for the rotor with one fully broken bar, and −23 dB for the rotor with three fully broken bars (Fig. 23).

Finally, it can be observed that the proposed method is effective not only for BRBs detection but also for a reliable classification of the rotor cage condition. The greater is the normalised magnitude of the BRB-related current spectral component, the greater is the rotor cage fault severity, as experimentally clarified in Fig. 23.

Although the proposed method has been verified on the inverter-fed SCIM, it has to be pointed out that the previously obtained results also hold for line-connected SCIMs equipped with an adequate DC injection braking module. Note that before applying the DC injection braking, the AC voltage applied to the stator of the SCIM has to be disconnected. Therefore, the AC power source does not influence the proposed method.

In general, the proposed method can be applied for BRB detection and fault severity classification of SCIMs under arbitrary load conditions. However, the operating load will decrease the braking period, thus lowering the frequency resolution of the STFT. This slightly degrades the performance of the proposed method. For that reason, the proposed method is more suitable for high-inertia drives. Nevertheless,

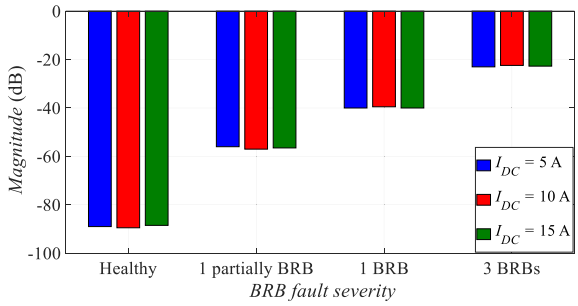

FIGURE 23. Average magnitudes of the BRB-related current spectral component with respect to the degree of the BRB fault and DC braking current values.

obtained results of the proposed method are valid regardless the load conditions.

V. CONCLUSION

A novel procedure for the BRB fault detection and identification of SCIM is presented. The approach combines the MCSA and DC injection braking methods, thus providing a new distinctive slip-independent BRB fault-related component in the motor current spectrum. Under these circumstances, this component and its characteristic time-frequency evolution pattern are extracted from the motor current signal and used as a BRB feature. To the best of our knowledge, the proposed approach is novel and has not been reported in literature.

The obtained results clearly reveal that the proposed methodology is highly effective and ensures accurate and reliable BRB detection, even under no-load operating conditions and one partially BRB. The magnitude of the BRB fault-related current component rapidly increases with the number of BRBs, thus enabling an easy distinction between healthy and faulty rotor cages, as well as evaluation of the fault severity. The results also reveal that the normalised value of the BRB fault-related current component is not influenced by the braking current value or machine load, which is also a significant benefit of the proposed methodology.

Considering that the DC injection braking can be easily integrated into the motor control system, the proposed BRB fault detection procedure is highly suitable for inverter-fed SCIM drives. Similarly, the method can also be implemented to line-connected SCIMs equipped with solid-state starters with DC injection braking, or line-connected SCIMs equipped with a DC injection braking module.

Further research may extend the proposed methodology by incorporating a DC signal injection strategy.

REFERENCES

[1] "Report of large motor reliability survey of industrial and commercial installations. Part I," *IEEE Trans. Ind. Appl.*, vol. IA-21, no. 4, pp. 853–864, Jul. 1985. [Online]. Available: https://ieeexplore.ieee.org/document/4158071

[2] "Report of large motor reliability survey of industrial and commercial installations. Part II," *IEEE Trans. Ind. Appl.*, vol. IA-21, no. 4, pp. 865–872, Jul. 1985. [Online]. Available: https://ieeexplore.ieee.org/document/4158072

[3] "Report of large motor reliability survey of industrial and commercial installations: Part 3," *IEEE Trans. Ind. Appl.*, vol. IA-23, no. 1, pp. 153–158, Jan. 1987. [Online]. Available: https://ieeexplore.ieee.org/document/4504880

[4] P. F. Albrecht, J. C. Appiarius, R. M. McCoy, E. L. Owen, and D. K. Sharma, "Assessment of the reliability of motors in utility applications—Updated," *IEEE Trans. Energy Convers.*, vol. EC-1, no. 1, pp. 39–46, Mar. 1986.

[5] O. V. Thorsen and M. Dalva, "A survey of faults on induction motors in offshore oil industry, petrochemical industry, gas terminals, and oil refineries," *IEEE Trans. Ind. Appl.*, vol. 31, no. 5, pp. 1186–1196, Sep./Oct. 1995.

[6] A. H. Bonnett, "Root cause failure analysis for AC induction motors in the petroleum and chemical industry," in *Proc. Rec. Conf. Papers Ind. Appl. Soc. 57th Annu. Petroleum Chem. Ind. Conf. (PCIC)*, Sep. 2010, pp. 1–13.

[7] A. Bellini, F. Filippetti, C. Tassoni, and G.-A. Capolino, "Advances in diagnostic techniques for induction machines," *IEEE Trans. Ind. Electron.*, vol. 55, no. 12, pp. 4109–4126, Dec. 2008.

[8] M. Garcia, P. A. Panagiotou, J. A. Antonino-Daviu, and K. N. Gyftakis, "Efficiency assessment of induction motors operating under different faulty conditions," *IEEE Trans. Ind. Electron.*, vol. 66, no. 10, pp. 8072–8081, Oct. 2019.

[9] Z. Gao, C. Cecati, and S. X. Ding, "A survey of fault diagnosis and fault-tolerant techniques: Fault diagnosis with model-based and signal-based approaches," *IEEE Trans. Ind. Electron.*, vol. 62, no. 6, pp. 3757–3767, Jun. 2015.

[10] D. Matić, Ž. Kanović, D. Reljić, F. Kulić, D. Oros, and V. Vasić, "Broken bar detection using current analysis—A case study," in *Proc. 9th IEEE Int. Symp. Diagnostic Electr. Mach., Power Electron. Drives (SDEMPED)*, Aug. 2013, pp. 407–411.

[11] J. A. Antonino-Daviu, A. Quijano-López, M. Rubbiolo, and V. Climente-Alarcon, "Advanced analysis of motor currents for the diagnosis of the rotor condition in electric motors operating in mining facilities," *IEEE Trans. Ind. Appl.*, vol. 54, no. 4, pp. 3934–3942, Jul. 2018.

[12] F. Filippetti, A. Bellini, and G. Capolino, "Condition monitoring and diagnosis of rotor faults in induction machines: State of art and future perspectives," in *Proc. IEEE Workshop Electr. Mach. Design, Control Diagnosis (WEMDCD)*, Paris, France, Mar. 2013, pp. 196–209.

[13] H. Henao, G.-A. Capolino, M. Fernandez-Cabanas, F. Filippetti, C. Bruzzese, E. Strangas, R. Pusca, J. Estima, M. Riera-Guasp, and S. Hedayati-Kia, "Trends in fault diagnosis for electrical machines: A review of diagnostic techniques," *IEEE Ind. Electron. Mag.*, vol. 8, no. 2, pp. 31–42, Jun. 2014.

[14] D. B. B. de Deus, C. A. N. Sobrinho, F. A. Belo, A. V. Brito, J. G. G. de Souza Ramos, and A. C. Lima-Filho, "Density of maxima approach for broken bar fault diagnosis in low slip and variable load conditions of induction motors," *IEEE Trans. Instrum. Meas.*, vol. 69, no. 12, pp. 9797–9804, Dec. 2020.

[15] R. Puche-Panadero, M. Pineda-Sanchez, M. Riera-Guasp, J. Roger-Folch, E. Hurtado-Perez, and J. Perez-Cruz, "Improved resolution of the MCSA method via Hilbert transform, enabling the diagnosis of rotor asymmetries at very low slip," *IEEE Trans. Energy Convers.*, vol. 24, no. 1, pp. 52–59, Mar. 2009.

[16] R. Puche-Panadero, J. Martinez-Roman, A. Sapena-Bano, J. Burriel-Valencia, M. Pineda-Sanchez, J. Perez-Cruz, and M. Riera-Guasp, "New method for spectral leakage reduction in the FFT of stator currents: Application to the diagnosis of bar breakages in cage motors working at very low slip," *IEEE Trans. Instrum. Meas.*, vol. 70, pp. 1–11, 2021.

[17] J. Martinez-Roman, R. Puche-Panadero, C. Terron-Santiago, A. Sapena-Bano, J. Burriel-Valencia, and M. Pineda-Sanchez, "Low-cost diagnosis of rotor asymmetries of induction machines at very low slip with the Goertzel algorithm applied to the rectified current," *IEEE Trans. Instrum. Meas.*, vol. 70, pp. 1–11, 2021.

[18] B. Asad, T. Vaimann, A. Belahcen, A. Kallaste, A. Rassõlkin, and M. N. Iqbal, "Broken rotor bar fault detection of the grid and inverter-fed induction motor by effective attenuation of the fundamental component," *IET Electric Power Appl.*, vol. 13, no. 12, pp. 2005–2014, Dec. 2019.

[19] A. Sapena-Baño, M. Pineda-Sanchez, R. Puche-Panadero, J. Martinez-Roman, and Ž. Kanović, "Low-cost diagnosis of rotor asymmetries in induction machines working at a very low slip using the reduced envelope of the stator current," *IEEE Trans. Energy Convers.*, vol. 30, no. 4, pp. 1409–1419, Dec. 2015.

[20] Y. Park, M. Jeong, S. B. Lee, J. A. Antonino-Daviu, and M. Teska, "Influence of blade pass frequency vibrations on MCSA-based rotor fault detection of induction motors," in *Proc. IEEE Energy Convers. Congr. Expo. (ECCE)*, Sep. 2016, pp. 1–8.

[21] S. B. Lee, D. Hyun, T.-J. Kang, C. Yang, S. Shin, H. Kim, S. Park, T.-S. Kong, and H.-D. Kim, "Identification of false rotor fault indications produced by online MCSA for medium-voltage induction machines," *IEEE Trans. Ind. Appl.*, vol. 52, no. 1, pp. 729–739, Jan. 2016.

[22] S. K. Ramu, G. C. R. Irudayaraj, S. Subramani, and U. Subramaniam, "Broken rotor bar fault detection using Hilbert transform and neural networks applied to direct torque control of induction motor drive," *IET Power Electron.*, vol. 13, no. 15, pp. 3328–3338, Nov. 2020.

[23] M. Pineda-Sanchez, R. Puche-Panadero, M. Riera-Guasp, J. Perez-Cruz, J. Roger-Folch, J. Pons-Llinares, V. Climente-Alarcon, and J. A. Antonino-Daviu, "Application of the Teager–Kaiser energy operator to the fault diagnosis of induction motors," *IEEE Trans. Energy Convers.*, vol. 28, no. 4, pp. 1036–1044, Dec. 2013.

[24] H. Li, G. Feng, D. Zhen, F. Gu, and A. D. Ball, "A normalized frequency-domain energy operator for broken rotor bar fault diagnosis," *IEEE Trans. Instrum. Meas.*, vol. 70, pp. 1–10, 2021.

[25] M. Malekpour, B. T. Phung, and E. Ambikairajah, "Stator current envelope extraction for analysis of broken rotor bar in induction motors," in *Proc. IEEE 11th Int. Symp. Diagnostics Electr. Mach., Power Electron. Drives (SDEMPED)*, Aug. 2017, pp. 240–246.

[26] G. Singh and V. N. A. Naikan, "Detection of half broken rotor bar fault in VFD driven induction motor drive using motor square current music analysis," *Mech. Syst. Signal Process.*, vol. 110, pp. 333–348, Sep. 2018.

[27] R. Puche-Panadero, J. Martinez-Roman, A. Sapena-Bano, and J. Burriel-Valencia, "Diagnosis of rotor asymmetries faults in induction machines using the rectified stator current," *IEEE Trans. Energy Convers.*, vol. 35, no. 1, pp. 213–221, Mar. 2020.

[28] D. Morinigo-Sotelo, R. D. J. Romero-Troncoso, P. A. Panagiotou, J. A. Antonino-Daviu, and K. N. Gyftakis, "Reliable detection of rotor bars breakage in induction motors via MUSIC and ZSC," *IEEE Trans. Ind. Appl.*, vol. 54, no. 2, pp. 1224–1234, Mar. 2018.

[29] Y. Trachi, E. Elbouchikhi, V. Choqueuse, and M. E. H. Benbouzid, "Induction machines fault detection based on subspace spectral estimation," *IEEE Trans. Ind. Electron.*, vol. 63, no. 9, pp. 5641–5651, Sep. 2016.

[30] B. Xu, L. Sun, L. Xu, and G. Xu, "Improvement of the Hilbert method via ESPRIT for detecting rotor fault in induction motors at low slip," *IEEE Trans. Energy Convers.*, vol. 28, no. 1, pp. 225–233, Mar. 2013.

[31] D. Camarena-Martinez, R. Osornio-Rios, R. J. Romero-Troncoso, and A. Garcia-Perez, "Fused empirical mode decomposition and MUSIC algorithms for detecting multiple combined faults in induction motors," *J. Appl. Res. Technol.*, vol. 13, no. 1, pp. 160–167, Feb. 2015.

[32] Y.-H. Kim, Y.-W. Youn, D.-H. Hwang, J.-H. Sun, and D.-S. Kang, "High-resolution parameter estimation method to identify broken rotor bar faults in induction motors," *IEEE Trans. Ind. Electron.*, vol. 60, no. 9, pp. 4103–4117, Sep. 2013.

[33] M. Mahmud and W. Wang, "A smart sensor-based cEMD technique for rotor bar fault detection in induction motors," *IEEE Trans. Instrum. Meas.*, vol. 70, pp. 1–11, 2021.

[34] K. N. Gyftakis and J. C. Kappatou, "The zero-sequence current as a generalized diagnostic mean in Δ-connected three-phase induction motors," *IEEE Trans. Energy Convers.*, vol. 29, no. 1, pp. 138–148, Mar. 2014.

[35] P. M. de la Barrera, M. Otero, T. Schallschmidt, G. R. Bossio, and R. Leidhold, "Active broken rotor bar diagnosis in induction motor drives," *IEEE Trans. Ind. Electron.*, vol. 68, no. 8, pp. 7556–7566, Aug. 2021.

[36] A. Sapena-Bano, J. Burriel-Valencia, M. Pineda-Sanchez, R. Puche-Panadero, and M. Riera-Guasp, "The harmonic order tracking analysis method for the fault diagnosis in induction motors under time-varying conditions," *IEEE Trans. Energy Convers.*, vol. 32, no. 1, pp. 244–256, Mar. 2017.

[37] M. Pineda-Sanchez, M. Riera-Guasp, J. Perez-Cruz, and R. Puche-Panadero, "Transient motor current signature analysis via modulus of the continuous complex wavelet: A pattern approach," *Energy Convers. Manage.*, vol. 73, pp. 26–36, Sep. 2013.

[38] P. A. Panagiotou, I. Arvanitakis, N. Lophitis, J. A. Antonino-Daviu, and K. N. Gyftakis, "FEM approach for diagnosis of induction machines' non-adjacent broken rotor bars by short-time Fourier transform spectrogram," *J. Eng.*, vol. 2019, no. 17, pp. 4566–4570, Jun. 2019.

[39] M. Riera-Guasp, M. Pineda-Sanchez, J. Perez-Cruz, R. Puche-Panadero, J. Roger-Folch, and J. A. Antonino-Daviu, "Diagnosis of induction motor faults via Gabor analysis of the current in transient regime," *IEEE Trans. Instrum. Meas.*, vol. 61, no. 6, pp. 1583–1596, Jun. 2012.
[40] A. L. Martinez-Herrera, L. M. Ledesma-Carrillo, M. Lopez-Ramirez, S. Salazar-Colores, E. Cabal-Yepez, and A. Garcia-Perez, "Gabor and the Wigner–Ville transforms for broken rotor bars detection in induction motors," in *Proc. Int. Conf. Electron., Commun. Comput. (CONIELECOMP)*, Feb. 2014, pp. 83–87.
[41] M. E. El-Dine Atta, D. K. Ibrahim, and M. I. Gilany, "Broken bar faults detection under induction motor starting conditions using the optimized stockwell transform and adaptive time–frequency filter," *IEEE Trans. Instrum. Meas.*, vol. 70, pp. 1–10, 2021.
[42] M. Lopez-Ramirez, C. Rodriguez-Donate, L. M. Ledesma-Carrillo, F. J. Villalobos-Pina, J. U. Munoz-Minjares, and E. Cabal-Yepez, "Walsh–Hadamard domain-based intelligent online fault diagnosis of broken rotor bars in induction motors," *IEEE Trans. Instrum. Meas.*, vol. 71, pp. 1–11, 2022.
[43] M. Lopez-Ramirez, L. M. Ledesma-Carrillo, F. M. Garcia-Guevara, J. Munoz-Minjares, E. Cabal-Yepez, and F. J. Villalobos-Pina, "Automatic early broken-rotor-bar detection and classification using Otsu segmentation," *IEEE Access*, vol. 8, pp. 112624–112632, 2020.
[44] V. Fernandez-Cavero, D. Morinigo-Sotelo, O. Duque-Perez, and J. Pons-Llinares, "A comparison of techniques for fault detection in inverter-fed induction motors in transient regime," *IEEE Access*, vol. 5, pp. 8048–8063, 2017.
[45] M. R. Mehrjou, N. Mariun, M. H. Marhaban, and N. Misron, "Rotor fault condition monitoring techniques for squirrel-cage induction machine—A review," *Mech. Syst. Signal Process.*, vol. 25, no. 8, pp. 2827–2848, Nov. 2011.
[46] D. G. Jerkan, D. D. Reljić, and D. P. Marčetić, "Broken rotor bar fault detection of IM based on the counter-current braking method," *IEEE Trans. Energy Convers.*, vol. 32, no. 4, pp. 1356–1366, Dec. 2017.
[47] T. A. Garcia-Calva, D. Morinigo-Sotelo, and R. D. J. Romero-Troncoso, "Non-uniform time resampling for diagnosing broken rotor bars in inverter-fed induction motors," *IEEE Trans. Ind. Electron.*, vol. 64, no. 3, pp. 2306–2315, Mar. 2017.
[48] T. A. Garcia-Calva, D. Morinigo-Sotelo, A. Garcia-Perez, D. Camarena-Martinez, and R. de Jesus Romero-Troncoso, "Demodulation technique for broken rotor bar detection in inverter-fed induction motor under non-stationary conditions," *IEEE Trans. Energy Convers.*, vol. 34, no. 3, pp. 1496–1503, Sep. 2019.
[49] M. A. Hmida and A. Braham, "Fault detection of VFD-fed induction motor under transient conditions using harmonic wavelet transform," *IEEE Trans. Instrum. Meas.*, vol. 69, no. 10, pp. 8207–8215, Oct. 2020.
[50] V. Fernandez-Cavero, J. Pons-Llinares, O. Duque-Perez, and D. Morinigo-Sotelo, "Detection of broken rotor bars in nonlinear startups of inverter-fed induction motors," *IEEE Trans. Ind. Appl.*, vol. 57, no. 3, pp. 2559–2568, May 2021.

DEJAN G. JERKAN (Member, IEEE) received the M.Sc. and Ph.D. degrees in electrical engineering from the University of Novi Sad, Serbia, in 2008 and 2016, respectively. Since 2014, he has been with the Faculty of Technical Sciences, University of Novi Sad, teaching courses in electrical machines. His research interests include motor fault diagnosis and numerical modeling of electrical machines.

DEJAN RELJIĆ (Member, IEEE) received the Ph.D. degree in electrical engineering from the Faculty of Technical Sciences, University of Novi Sad, Serbia, in 2017. He is currently an Assistant Professor with the Faculty of Technical Sciences, University of Novi Sad. His research interests include power electronics and its application in wireless power transfer technology, and control and fault diagnosis of electrical machines. He is a member of the IEEE Power Electronics Society and the IEEE Industrial Electronics Society.

IVAN TODOROVIĆ (Member, IEEE) received the M.Sc. and Ph.D. degrees in electrical engineering from the Faculty of Technical Sciences, University of Novi Sad, Serbia, in 2013 and 2018, respectively. He is currently an Assistant Professor with the Faculty of Technical Sciences, University of Novi Sad. His research interests include problems related to integration of power electronics devices with power systems, especially mechanisms for power systems disturbances handling and mitigation utilizing the power electronics devices, and emerging technologies regarding electric vehicles. He is a member of the IEEE Industry Applications Society and the IEEE Industrial Electronics Society.

IVANA ISAKOV (Member, IEEE) received the B.Sc. and M.Sc. degrees from the Faculty of Technical Sciences, University of Novi Sad, Serbia, in 2015 and 2016, respectively, with a major in the field of the control of grid-connected power converters, where she is currently pursuing the Ph.D. degree. She is also currently working as a Teaching Assistant with the Faculty of Technical Sciences, University of Novi Sad. Her research interests include in the domain of power electronics control applied to the distributed energy sources and distribution grids and microgrids. Particularly, she is interested in distributed control of modern power grids. She is a member of the IEEE Industry Applications Society and the IEEE Industrial Electronics Society.

VLADO POROBIĆ (Member, IEEE) received the B.Sc., M.Sc., and Ph.D. degrees in electrical engineering from the Faculty of Technical Sciences, University of Novi Sad, Serbia, in 2000, 2005, and 2012, respectively. He is employed at the Faculty of Technical Sciences, University of Novi Sad, as an Associate Professor with the Department of Power, Electronics and Telecommunication Engineering. During his career, he has worked on various projects in the field of electrical drives, control of power converters in renewable energy applications, and the development of HIL emulator devices. His main research interest includes digital control of electric machines.

DRAŽEN DUJIĆ (Senior Member, IEEE) received the Dipl.-Ing. and M.Sc. degrees from the University of Novi Sad, Novi Sad, Serbia, in 2002 and 2005, respectively, and the Ph.D. degree from Liverpool John Moores University, Liverpool, U.K., in 2008, all in electrical engineering. From 2002 to 2006, he was a Research Assistant with the Department of Power, Electronics and Telecommunication Engineering, University of Novi Sad. From 2006 to 2009, he was a Research Associate with Liverpool John Moores University. From 2009 to 2013, he was the Principal Scientist with ABB Corporate Research Centre, Baden, Switzerland; and the Research and Development Platform Manager with ABB Medium Voltage Drives, Turgi, Switzerland, from 2013 to 2014. He is currently an Associate Professor and the Director of the Power Electronics Laboratory, École Polytechnique Fédérale de Lausanne, Lausanne, Switzerland. He has published more than 200 scientific publications and has filed 18 patents (some pending). His current research interest includes design and control of advanced high-power electronics systems for medium-voltage applications. He was a recipient of the First Prize Paper Award from the Electric Machines Committee of the IEEE Industrial Electronics Society, in 2007; the Isao Takahashi Power Electronics Award for outstanding achievement in power electronics, in 2014; and the EPE Outstanding Service Award from the European Power Electronics and Drives Association, in 2018. He is an Associate Editor of IEEE TRANSACTIONS ON INDUSTRIAL ELECTRONICS, IEEE TRANSACTIONS ON POWER ELECTRONICS, and *IET Electric Power Applications*.